

# High-Order Triangle-based Discontinuous Galerkin Methods for Hyperbolic Equations on a Rotating Sphere

Francis X. Giraldo

*Naval Research Laboratory, Monterey, CA 93943, USA*

**Journal of Computational Physics**

Submitted April 5, 2005

---

High-order triangle-based discontinuous Galerkin (DG) methods for hyperbolic equations on a rotating sphere are presented. The DG method can be characterized as the fusion of finite elements with finite volumes. This DG formulation uses high-order Lagrange polynomials on the triangle using nodal sets up to 15th order. The finite element-type area integrals are evaluated using order  $2N$  Gauss cubature rules. This leads to a full mass matrix which, unlike for continuous Galerkin (CG) methods such as the spectral element (SE) method presented in [16], is small, local and efficient to invert. Two types of finite volume-type flux integrals are studied: a set based on Gauss-Lobatto quadrature points (order  $2N - 1$ ) and a set based on Gauss quadrature points (order  $2N$ ). Furthermore, we explore conservation and advection forms as well as strong and weak forms. Seven test cases are used to compare the different methods including some with scale contractions and shock waves. All three strong forms performed extremely well with the strong conservation form with  $2N$  integration being the most accurate of the four DG methods studied. The strong advection form with  $2N$  integration performed extremely well even for flows with shock waves. The strong conservation form with  $2N - 1$  integration yielded results almost as good as those with  $2N$  while being less expensive. All the DG methods performed better than the SE method for almost all the test cases, especially for those with strong discontinuities. Finally, the DG methods required less computing time than the SE method due to the local nature of the mass matrix.

---

*Key Words:* Dubiner, electrostatics, Fekete, finite element, finite volume, Jacobi, Koornwinder, Lagrange, penalty method, polynomial, Prorior, Riemann solver, Rusanov flux, shallow water equations, spherical geometry.



## 1. INTRODUCTION

On spherical domains, the most natural solution strategy is to use spherical harmonics (spectral transform methods) on a Gaussian grid where the longitude and latitude are the spherical coordinates. However, choosing spherical harmonics eliminates any possibility of exploiting adaptive solution strategies. Furthermore, for solving relevant problems the numerical model must be run in a distributed-memory mode (such as with the Message-Passing Interface). It is well known that the cost of spherical harmonics is  $O(N_{lat}^3)$  where  $N_{lat}$  denotes the number of grid points in the latitudinal direction (south to north pole).

On the other hand, local methods (e.g., finite differences, elements, and volumes) cost on the order of  $O(N_p^2)$  where  $N_p$  denotes the number of total grid points. If either adaptivity or unstructured grids are to be used then this now only leaves finite elements (FE) and finite volumes (FV) as the only two viable options. Typically, a choice has had to be made between high order accuracy and local conservation.

If high order accuracy (beyond 2nd order) is selected as the main criterion then the FE method must be the method selected. High order FE methods are typically referred to as spectral elements (SE) and we shall use these two terms interchangeably throughout this manuscript. FE/SE methods have shown to be quite capable of producing very accurate solutions for flows on rotating spheres (see [16]) provided that the solutions are smooth. However, if the solutions are non-smooth then FE/SE methods do not perform as well. We showed this in [13] in the context of unstructured quadrilateral elements and we show this in Sec. 5 for unstructured triangular elements.

However, if local conservation is the main criterion then FV methods must be chosen. FV methods have been shown to be quite effective in handling discontinuous flows on rotating spheres (see [23]). However, FV methods are at most second order accurate on unstructured triangular grids (see [10]); higher order reconstructions are only readily available for Cartesian (structured) grids and only using quadrilaterals.

Thus if both high order accuracy and local conservation on unstructured triangular grids are sought then the natural choice is the discontinuous Galerkin (DG) method. In essence, the DG method extracts the best features of FE and FV methods and fuses them into a powerful method capable of delivering high order accuracy in conjunction with local conservation. In [13] we introduced the first DG formulation for flows on a rotating sphere using much of the same machinery originally developed for SE methods (see [12]); the main difference being that we replaced the  $C^0$  continuity condition of SE methods with a discontinuity at the element interfaces resolved via jump conditions in a similar vein to that of penalty methods (see [4]). Because the DG method shares much in common with FV methods then much of the same machinery developed for FV methods such as total variation diminishing (TVD) schemes and nonlinear flux limiters can be applied to DG methods which then renders the solutions not only high-order accurate but also monotonicity preserving as well.

In addition to offering local conservation, high order accuracy, monotonicity, and adaptivity, the DG method also offers efficiency and natural *parallelization* especially for unstructured triangular grids. To clarify this point, in Fig. 1 we show the discrete stencil required by both the DG and SE methods. The DG stencil



is shown by the solid triangles (3 triangles) and the SE stencil by both the solid and dashed triangles (13 triangles). Note that no matter how unstructured the grid becomes, the DG triangle will always have only 3 edge neighbors (E1, E2, and E3) to communicate with while the communication stencil of the SE triangle is much larger because the  $C^0$  continuity condition is based on vertex neighbors. With grid adaptivity, the number of vertex neighbors for the SE triangle may change drastically from one grid generation to the next whereas the DG triangle will always have only three edge neighbors no matter how distorted the grid becomes.

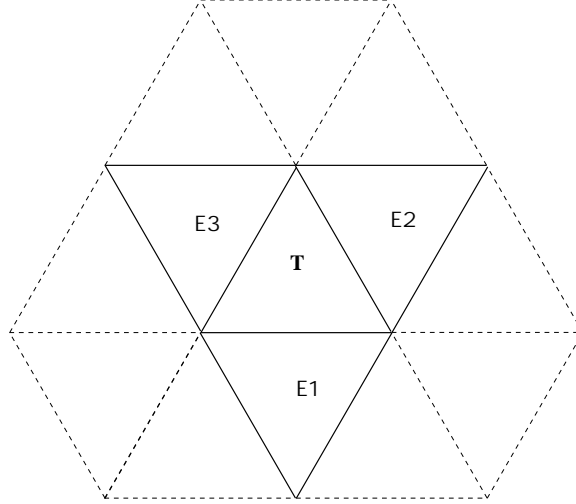


**FIG. 1.** The discrete stencil of the triangle,  $T$ , for the DG method (solid triangles) and the SE method (solid and dashed triangles).

It should be mentioned that recently robust high-order (3rd order) FV using weighted essentially non-oscillatory (WENO) reconstructions have been developed (see [8], [18], [24]) for unstructured triangular grids. There exists a 4th order reconstruction (see [18]) but it is not as geometrically flexible as its lower order cousins. WENO FV methods show great promise and higher order reconstructions are underway but the complexity in constructing the weighted differencing stencils may prove to be too daunting a task. The advantage that DG methods have over WENO FV and all other methods is that DG methods can be used on highly unstructured triangulations and to arbitrarily high order. Nonetheless, the DG method is not without its weakness; current research in DG methods focuses on the construction of robust TVD limiters for shock wave phenomena which we reserve for future work.

The remainder of the paper is organized as follows. Section 2 describes the governing equations of motion used to test our numerical method. In Sec. 3 we describe the discretization of the governing equations. This includes the spatial discretization by the triangle-based DG method and the time-integrator. In Sec. 4 we describe one of the many possible triangulations on a sphere. Finally, in Sec. 5 we present convergence rates for the four triangle-based DG methods and compare them with the SE method. This then leads to some conclusions about the



performance of the various DG methods studied and a discussion on the direction of future work.

## 2. CONTINUOUS EQUATIONS

The discontinuous Galerkin method we propose in this work is applicable to any nonlinear hyperbolic partial differential equation on a sphere. Thus at this point the only condition on the continuous equations is that the flow be inviscid - that is, the method is equally applicable to the Euler, shallow water, and magneto-hydrodynamics shallow water equations. For the purposes of describing the algorithm we shall restrict our attention to the shallow water equations; in future work we shall address other equation sets.

The shallow water equations are a system of first order nonlinear hyperbolic equations which govern the motion of an inviscid incompressible fluid in a shallow depth. The predominant feature of this type of fluid is that the characteristic length of the fluid is far greater than its depth which is analogous to the motion of air in the atmosphere and water in the oceans. For this reason these equations are typically used as a first step toward the construction of either NWP, climate, or ocean models.

The shallow water equations on a sphere in Cartesian conservation form are

$$\frac{\partial \mathbf{q}}{\partial t} + \nabla \cdot \mathbf{F}(\mathbf{q}) = S(\mathbf{q}) \quad (1)$$

where  $\mathbf{q} = (\phi, \phi \mathbf{u}^T)^T$  are the conservation variables,

$$\mathbf{F}(\mathbf{q}) = \begin{pmatrix} \phi \mathbf{u} \\ \phi \mathbf{u} \otimes \mathbf{u} + \frac{1}{2} \phi^2 \mathcal{I}_3 \end{pmatrix} \quad (2)$$

is the flux tensor and

$$S(\mathbf{q}) = - \begin{pmatrix} 0 \\ f(\mathbf{x} \times \phi \mathbf{u}) + \phi \nabla \phi^s + \mu \mathbf{x} \end{pmatrix} \quad (3)$$

is the source function where the nabla operator is defined as  $\nabla = (\partial_x, \partial_y, \partial_z)^T$ ,  $\otimes$  denotes the tensor product operator,  $\phi$  is the geopotential height ( $\phi = gh$  where  $g$  is the gravitational constant and  $h$  is the vertical height of the fluid),  $\phi^s$  is the surface topography (e.g., mountains),  $\mathbf{u} = (u, v, w)^T$  is the Cartesian wind velocity vector,  $f = \frac{2\omega z}{a^2}$  is the Coriolis parameter and  $(\omega, a)$  represent the rotation of the earth and its radius, respectively. The term  $\mathcal{I}_3$  is a rank-3 identity matrix, and the term  $\mu \mathbf{x}$ , where  $\mathbf{x} = (x, y, z)^T$  is the position vector of the grid points, is a fictitious force introduced to constrain the fluid particles to remain on the surface of the sphere. Switching from spherical (2D) to Cartesian (3D) coordinates allows the fluid particles an additional degree of freedom; the Lagrange multiplier,  $\mu$ , is introduced in order to prevent particles from flying off the sphere. The reason for using the Cartesian form of the equations is that the pole singularity associated with spherical coordinates is avoided and because this form, in conjunction with the mapping described in Sec. 3.1.1, allows for any curved surface to be discretized by this approach.



Alternatively, Eq. (1) can be recast in the advection form

$$\frac{\partial \mathbf{q}^A}{\partial t} + \mathbf{u} \cdot \nabla \mathbf{q}^A + \nabla \mathbf{p} = S(\mathbf{q}^A) \quad (4)$$

where  $\mathbf{q}^A = (\phi, \mathbf{u}^T)^T$  is the solution vector,  $\mathbf{p} = (0, \phi, \phi, \phi)^T$  is the pressure vector, and

$$S(\mathbf{q}^A) = - \begin{pmatrix} \phi \nabla \cdot \mathbf{u} \\ f(\mathbf{x} \times \mathbf{u}) + \nabla \phi^s + \mu \mathbf{x} \end{pmatrix} \quad (5)$$

is the source function. The reason for considering the advection form of the equations is because we would like to be able to use semi-Lagrangian time-integrators (see [14]) in future work.

### 3. DISCRETIZATION

In this section we describe the discretization of the shallow water equations. In Sec. 3.1, we describe the spatial discretization by the discontinuous Galerkin method including: the choice of basis functions, integration, and construction of the semi-discrete problem using various DG formulations. In Sec. 3.2 we describe the explicit time-integrator.

#### 3.1. Triangle-based Discontinuous Galerkin Method

##### 3.1.1. Basis Functions

To define the discrete local operators we begin by decomposing the spherical domain  $\Omega$  into  $N_e$  conforming non-overlapping triangular elements  $\Omega_e$  such that

$$\Omega = \bigcup_{e=1}^{N_e} \Omega_e.$$

It should be mentioned, however, that the condition on grid conformity is not required by the DG method; we only impose this condition for ease of exposition.

To perform differentiation and integration operations, we introduce the non-singular mapping  $\mathbf{x} = \Psi(\boldsymbol{\xi})$  which defines a transformation from the physical Cartesian coordinate system  $\mathbf{x} = (x, y, z)^T$  to the local reference coordinate system  $\boldsymbol{\xi} = (\xi, \eta, \zeta)^T$  such that  $(\xi, \eta)$  lies on the spherical surface tiled by the triangular elements defined by  $\Omega_e = \{(\xi, \eta, \zeta), -1 \leq \xi, \eta \leq 1, \xi + \eta \leq 0, \zeta = 1\}$ .

Let us now represent the local element-wise solution  $\mathbf{q}$  by an  $N$ th order polynomial in  $\boldsymbol{\xi}$  as

$$\mathbf{q}_N(\boldsymbol{\xi}) = \sum_{i=1}^{M_N} L_i(\boldsymbol{\xi}) \mathbf{q}_N(\boldsymbol{\xi}_i) \quad (6)$$

where  $\boldsymbol{\xi}_i$  represents  $M_N = \frac{1}{2}(N+1)(N+2)$  grid points and  $L_i(\boldsymbol{\xi})$  are the associated multivariate Lagrange polynomials. For the grid points  $\boldsymbol{\xi}_i$  we choose the nodal set derived from the electrostatics principle [17] for  $N < 11$  and the Fekete points [26] for  $11 \leq N \leq 15$ . These sets were selected because they yield the lowest Lebesgue constants currently found in the literature. In [16] these nodal sets were shown to exhibit exponential convergence for the shallow water equations on the sphere using a spectral element formulation. The details on the construction of the



Lagrange polynomial basis functions can be found in [16] where cardinal functions based on the Proriot-Koornwinder-Dubiner (PKD) polynomials [22, 20, 5] are used. Alternatively, one could also choose to use the PKD polynomials themselves as the basis functions as is done in [7] and [6] which then yields a modal representation (spectral or amplitude-frequency space) of the solution variables instead of the nodal representation (physical space) that we propose. Both the modal and nodal representations should yield the same accuracy; however, the difference between these two forms may be in their relative efficiencies (i.e., computational cost). In the future, comparison studies between these two forms should be performed in order to quantify their performance but for now we shall proceed only with the nodal representation.

### 3.1.2. Integration

In order to complete the discussion of the local element-wise operations required to construct discrete spatial operators we must lastly describe the integration procedure required by the weak formulation of all Galerkin methods. For any two functions  $f$  and  $g$  the integration  $\mathcal{I}$  proceeds as follows

$$\mathcal{I}[f, g] = \int_{\Omega_e} f(\mathbf{x}) g(\mathbf{x}) d\mathbf{x} = \sum_{i=1}^{M_Q} w_i |J(\boldsymbol{\xi}_i)| f(\boldsymbol{\xi}_i) g(\boldsymbol{\xi}_i)$$

where  $M_Q$  is a function of  $Q$  which represents the order of the cubature approximation. For  $w_i$  and  $\boldsymbol{\xi}_i$  we use the high-order cubature rules for the triangle given in [25, 2, 21, 3]. We are now in a position to construct the semi-discrete problem.

### 3.1.3. Tangent and Normal Vectors of the Element Edges

Below it will become evident that in order to construct a discontinuous Galerkin discretization requires knowing a bit about the element geometry. In continuous Galerkin methods such as finite and spectral element methods the only required information is the basis functions, metric terms, and cubature rules. The DG method requires all of this finite element-type information plus some finite volume-type information regarding the element edges and the element neighbors sharing these edges. However, the good news for the DG method is that regardless of the order of the basis function,  $N$ , each element only has three edge neighbors. This is the process by which a DG element shares its local information with its neighbors. Figure 2 shows a schematic of a master element along with its three normal vectors. Note that the tangent vectors for the three edges are given as follows:

- for edge 1  $\mathbf{t}_1 = \frac{\partial \mathbf{x}}{\partial \xi}$
- for edge 2  $\mathbf{t}_2 = -\frac{\partial \mathbf{x}}{\partial \xi} + \frac{\partial \mathbf{x}}{\partial \eta}$
- for edge 3  $\mathbf{t}_3 = -\frac{\partial \mathbf{x}}{\partial \eta}$

Now, let  $\mathbf{r} = \frac{\mathbf{x}}{a}$  be the radial vector oriented from the origin (the center of the sphere) to the point  $\mathbf{x}$ ; on the master element given in Fig. 2  $\mathbf{r}$  points out of the paper. Then the normal vectors are computed as follows  $\mathbf{n} = \mathbf{t} \times \mathbf{r}$  which then must be normalized to unity. Although the radial vector,  $\mathbf{r}$ , and the tangent vector,  $\mathbf{t}$ , change along an edge its cross product,  $\mathbf{n}$ , remains constant throughout; thus we



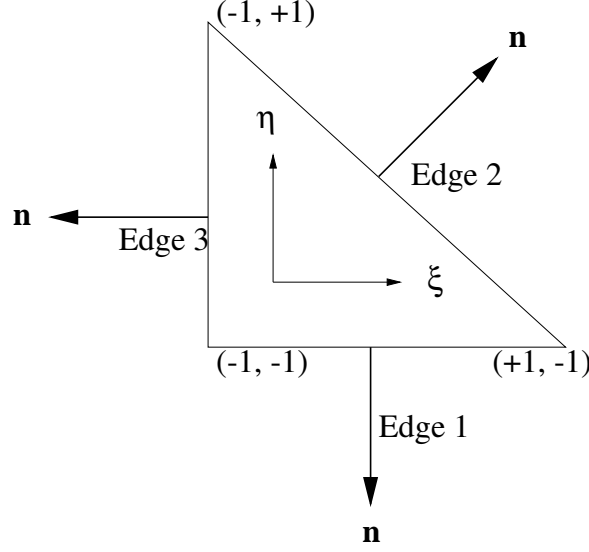


**FIG. 2.** The normal vectors of the master triangle.

only need to store one normal vector per edge regardless of the number of cubature points along that edge.

### 3.1.4. Conservation Form

Applying the discontinuous Galerkin discretization to the conservation form, Eq. (1), and using Green's theorem yields the classical DG form which we shall refer to as the *weak conservation* form

$$\int_{\Omega_e} \left( \frac{\partial \mathbf{q}_N}{\partial t} - \mathbf{F}_N \cdot \nabla - S_N \right) L_i(\mathbf{x}) d\mathbf{x} = - \int_{\Gamma_e} L_i(\mathbf{x}) \mathbf{n} \cdot \mathbf{F}_N^* d\mathbf{x} \quad (7)$$

where  $f_N$  is the polynomial representation of any function  $f$  given by Eq. (6) and  $\mathbf{n}$  is the outward pointing normal vector of the element edge  $\Gamma_e$ .  $\mathbf{F}_N^*$  is the Rusanov numerical flux

$$\mathbf{F}_N^* = \frac{1}{2} [\mathbf{F}_N(\mathbf{q}_N^L) + \mathbf{F}_N(\mathbf{q}_N^R) - |\lambda| (\mathbf{q}_N^R - \mathbf{q}_N^L) \mathbf{n}] \quad (8)$$

where  $\lambda = \max(U^L + \sqrt{\phi^L}, U^R + \sqrt{\phi^R})$  with  $U^{L,R} = \mathbf{u}^{L,R} \cdot \mathbf{n}$  being the normal component of velocity with respect to the edge  $\Gamma_e$ , and the superscripts  $L$  and  $R$  represent the left and right states of the element edge. The normal vector  $\mathbf{n}$  is defined as pointing outward from left to right. Numerous other numerical fluxes are possible (such as those based on either exact or approximate Riemann solvers) but we have chosen the Rusanov flux primarily due to its generality and simplicity. In future work we shall explore different fluxes in connection with total variation diminishing (TVD) schemes.

Integrating Eq. (7) by parts once more yields the *strong conservation* form

$$\int_{\Omega_e} L_i(\mathbf{x}) \left( \frac{\partial \mathbf{q}_N}{\partial t} + \nabla \cdot \mathbf{F}_N - S_N \right) d\mathbf{x} = \int_{\Gamma_e} L_i(\mathbf{x}) \mathbf{n} \cdot (\mathbf{F}_N - \mathbf{F}_N^*) d\mathbf{x} \quad (9)$$



which, although mathematically equivalent to the weak form, yields different numerical solutions.

*Remark.* In [13] we referred to the *strong*, Eq. (9), and *weak*, Eq. (7), conservation forms as the *divergence* and *Green's* forms. In addition, we referred to the Rusanov flux, Eq. (8), as the Lax-Friedrichs flux. These two fluxes are equivalent if and only if the maximum wave speed,  $\lambda$ , approaches the Courant number which need not always be the case (e.g., see [27]).

### 3.1.5. Advection Form

Applying the discontinuous Galerkin discretization to the advection form, Eq. (4), and using Green's theorem yields the *weak advection* form

$$\int_{\Omega_e} \left( \frac{\partial q_N^A}{\partial t} - \mathbf{F}_N^A \cdot \nabla - \mathbf{q}^A \nabla \cdot \mathbf{u} - S_N^A \right) L_i(\mathbf{x}) d\mathbf{x} = - \int_{\Gamma_e} L_i(\mathbf{x}) \mathbf{n} \cdot \mathbf{F}_N^{A,*} d\mathbf{x} \quad (10)$$

where

$$\mathbf{F}_N^A = \begin{pmatrix} \phi_N \mathbf{u}_N \\ \mathbf{u}_N \otimes \mathbf{u}_N + \phi_N \mathcal{I}_3 \end{pmatrix} \quad (11)$$

is the flux tensor corresponding to the advection form of the equations.

Integrating Eq. (10) by parts once more yields the *strong advection* form

$$\int_{\Omega_e} L_i(\mathbf{x}) \left( \frac{\partial q_N^A}{\partial t} + \mathbf{u}_N \cdot \nabla q_N^A + \nabla p_N - S_N^A \right) d\mathbf{x} = \int_{\Gamma_e} L_i(\mathbf{x}) \mathbf{n} \cdot (\mathbf{F}_N^A - \mathbf{F}_N^{A,*}) d\mathbf{x}. \quad (12)$$

*Remark.* The weak form of the DG, Eqs. (7) and (10), is easier to implement numerically because this form does not require constructing derivatives of the flux tensors, only the derivatives of the basis functions.

*Remark.* The strong form, Eqs. (9) and (12), is conceptually more attractive, and somewhat reminiscent of penalty methods, in that it amounts to satisfying the original equations in a local element sense with neighboring elements communicating only via the penalty/jump conditions represented by the flux terms on the right-hand-side of the equations. This is evident by comparing Eqs. (1) and (9), and Eqs. (4) and (12).

*Remark.* Conventional wisdom discourages the use of the advection form for finite volume methods. The reason given is that this form is not guaranteed to converge to the correct solution when strong shocks are present. We study the DG in strong advection form to see if for the limited number of cases we study we see such behavior.

## 3.2. Time-Integrator

In almost all DG formulations, the time-integrator is usually chosen to be some variant of Runge-Kutta (RK) methods. This family of time-integrators is selected because these methods are stable for eigenvalues off the imaginary axis. However, in many applications in geophysical fluid dynamics (GFD) semi-implicit methods



based on second order leapfrog (LF2) have been the method of choice; however, LF2 does not work very well for DG precisely because the DG eigenvalues are more akin to parabolic equations rather than purely hyperbolic systems. Since the DG method proposed in the present work is meant to appeal to researchers in both computational fluid dynamics (CFD) and GFD we shall use an explicit version of the second order backward difference formula (BDF2) originally proposed by Karniadakis et al. (see [19]).

For the set of ordinary differential equations

$$\frac{\partial \mathbf{q}}{\partial t} = \mathbf{R} \quad (13)$$

the explicit BDF2 time-integrator yields:

$$\mathbf{q}^{n+1} = \frac{4}{3}\mathbf{q}^n - \frac{1}{3}\mathbf{q}^{n-1} + \frac{4}{3}\Delta t \mathbf{R}^n - \frac{2}{3}\Delta t \mathbf{R}^{n-1} \quad (14)$$

which, like RK methods, is stable for eigenvalues off the imaginary axis and is therefore as stable as RK but is a one-stage three-time-level method. We have used this method quite successfully for semi-implicit hydrostatic primitive equation models [15] and semi-Lagrangian shallow water models [14]. It turns out that the explicit BDF2 and RK2 have similar stability regions; however, the fact that BDF2 only requires one evaluation of the discrete operators per time step means that it is more efficient than RK2.

#### 4. TRIANGULATION ON A SPHERE

The choice of which triangulation to use for the sphere is not obvious. Commonly, grids are chosen which simplify the construction of the discrete operators. For example, latitude-longitude grids are used with spectral transform methods because these are the only grids that can be used with this method. The hexahedral grid (i.e., the cubed-sphere) has been used with finite difference, finite volume, and spectral element methods because each of the six faces of the cube map onto a simple Cartesian geometry that allows for the simple and rapid construction of the discrete operators. Picking one grid and constructing the discrete operators on a specific grid geometry simplifies matters but it also dictates the algorithm thereby losing any hope of using other types of grids and adaptive solution strategies.

In our case, the DG method is constructed in a very general way such that the model reads in any grid geometry and then constructs the discrete operators directly on the grid. This allows the use of any grid and offers the freedom to choose the best possible grid for specific applications. For the purposes of validating the triangle-based DG methods we shall use a disjointed set of triangles formed by the subdivision of the triangular faces of an icosahedron; however, it should be understood that any triangular grid can be used; other possible triangulations are presented in [16].

To construct icosahedral grids we consider the initial icosahedron and subdivide each of the initial triangles by a Lagrange polynomial of order  $n_I$ . Prior to mapping these elements onto the sphere it is convenient to map the triangles onto a gnomonic space. The most unbiased mapping is obtained by mapping about the centroid of the triangles.



Let  $(\lambda_c, \theta_c)$  be the centroid of the triangle we wish to map where  $\lambda$  represents the zonal (east-west) and  $\theta$  the meridional (north-south) directions. The gnomonic mapping is then given by

$$\begin{aligned} X &= \frac{a \cos \theta \sin(\lambda - \lambda_c)}{\sin \theta_c \sin \theta + \cos \theta_c \cos \theta \cos(\lambda - \lambda_c)}, \\ Y &= \frac{a [\cos \theta_c \sin \theta - \sin \theta_c \cos \theta \cos(\lambda - \lambda_c)]}{\sin \theta_c \sin \theta + \cos \theta_c \cos \theta \cos(\lambda - \lambda_c)} \end{aligned} \quad (15)$$

where  $\mathbf{X} \in [-1, +1]^2$  in the equi-distant gnomonic space  $G$ . To simplify matters a bit, we first apply a rotation whereby Eq. (15) becomes

$$X = a \tan \lambda_R, \quad Y = a \tan \theta_R \sec \lambda_R,$$

in the new coordinate system with the centroid  $(\lambda_c, \theta_c)$  located at  $(0, 0)$ . The rotation mapping is given as

$$\begin{aligned} \lambda_R &= \arctan \left[ \frac{\cos \theta \sin(\lambda - \lambda_c)}{\sin \theta_c \sin \theta + \cos \theta_c \cos \theta \cos(\lambda - \lambda_c)} \right], \\ \theta_R &= \arcsin [\cos \theta_c \sin \theta - \sin \theta_c \cos \theta \cos(\lambda - \lambda_c)]. \end{aligned}$$

This approach enables the construction of an icosahedral grid with the following properties

$$N_p = 10(n_I N)^2 + 2, \quad (16)$$

$$N_e = 20(n_I)^2, \quad (17)$$

where  $N_p$  and  $N_e$  denote the number of points and elements comprising the triangular grid, and  $n_I$  controls the number of triangular elements while  $N$  denotes the order of the polynomial inside each element. Figure 3 provide examples of grids for

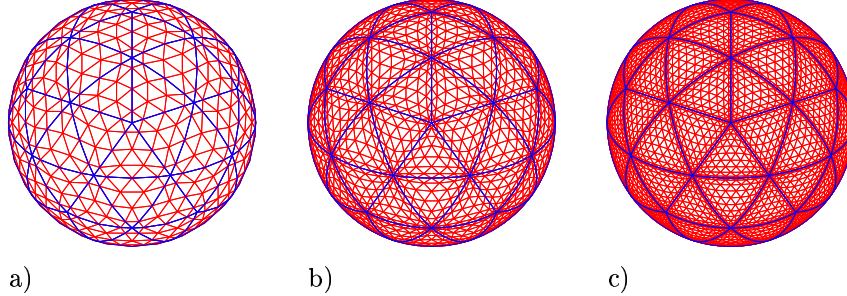


**FIG. 3.** Icosahedral grid for  $n_I = 2$  and a)  $N = 4$ , b)  $N = 8$ , and c)  $N = 12$ .

$n_I = 2$  and  $N = 4, 8$  and  $12$ . All the grids illustrated are viewed from the North Pole where the thick lines denote the elements and the thin lines are the high-order grid points.

## 5. NUMERICAL EXPERIMENTS



For the numerical experiments, we use the normalized  $L_2$  error norm

$$\|\phi\|_{L_2} = \sqrt{\frac{\int_{\Omega} (\phi_{\text{exact}} - \phi)^2 d\Omega}{\int_{\Omega} \phi_{\text{exact}}^2 d\Omega}}$$

to judge the accuracy of the SE methods. To compute the Courant number the elements are decomposed into their high-order (HO) grid points and these grid points form a fine grid which we refer to as the HO cells. The velocities and grid spacings are then defined at the centers of these cells. Using these definitions the Courant number is then defined as

$$\text{Courant number} = \max \left( \frac{C \Delta t}{\Delta s} \right)_{HO}^e \quad \forall e \in [1, \dots, N_e]$$

where

$$C = \begin{cases} U & \text{for cases 1 and 5} \\ U + \sqrt{\phi} & \text{for cases 2, 3, 4, and 6} \end{cases}$$

where  $C$  is the characteristic speed,  $U = \sqrt{\mathbf{u} \cdot \mathbf{u}}$ , and  $\Delta s = \sqrt{\Delta x^2 + \Delta y^2 + \Delta z^2}$  is the grid spacing. For all the results presented the Courant number is taken to be  $\leq 0.2$  which is the region of stability for BDF2 (see [15]).

Seven test cases are used to judge the performance of the triangle-based DG methods. Cases 1, 2, and 3 correspond to the Williamson et al. standard test case suite [28]. Case 4 was recently proposed by Galewsky et al. for testing shallow water models [9]. This case presents a more challenging test than those in the Williamson et al. test suite because if the resolution is not sufficiently high then the numerics will not be able to sustain the steady zonal jet with steep vorticity gradient. If the method cannot sustain the jet then the accuracy declines rapidly. Cases 1 through 4 represent solutions which are free of shocks or steep gradients. Cases 5, 6, and 7 are good for testing the ability of a numerical method to handle discontinuities.

### 5.1. Description of the Test Cases

#### 5.1.1. Case 1: Passive Advection of a Cosine Wave

Case 1 concerns the solid body rotation of a cosine wave. The velocity field remains unchanged throughout the computation. Williamson et al. [28] recommend that the error be computed after 12 days of integration which corresponds to one complete revolution of the cosine wave.

#### 5.1.2. Case 2: Steady-State Nonlinear Zonal Geostrophic Flow

This case is a steady-state solution to the nonlinear shallow water equations. The equations are geostrophically balanced and remain so for the duration of the integration where the velocity field remains constant throughout the computation. The geopotential height  $\phi$  undergoes a solid body rotation but since the initial height field is given as a constant band in the zonal direction and the flow field is purely zonal, then the solution remains unchanged throughout the time-integration. The velocity field is the same as that used in case 1. Williamson et al. [28] recommend that the error be computed after 5 days.

#### 5.1.3. Case 3: Steady-State Nonlinear Zonal Geostrophic Flow with Compact Support



This case is another steady-state solution to the nonlinear shallow water equations where the equations remain geostrophically balanced for the duration of the integration. The initial velocity field is zero everywhere except in a very small isolated region. This isolated region, or jet, encapsulates the flow and confines the geopotential height field to remain within a localized circular region. The results are reported for a 5-day integration as suggested in [28].

#### 5.1.4. Case 4: Galewsky et al. Zonal Dynamics

This test case consists of a zonal jet and an unperturbed balanced initial geopotential height field. The balanced initial field should be maintained indefinitely but Galewsky et al. [9] suggest running the case for 5 days. This is a rather stringent test of shallow water models because if the accuracy and/or the resolution is not sufficiently high then the model will not be able to sustain the balanced initial field and the error will increase quite rapidly, unlike cases 1, 2, and 3 which are much more forgiving. In addition, because the jet is zonally positioned, then any grid that is not aligned with the zonal direction will have much more difficulty maintaining the jet.

#### 5.1.5. Case 5: Passive Advection of a Cylinder

This test case is similar to case 1 except that the cosine wave is replaced by a cylinder which is essentially the 2D analog of the 1D square pulse problem. This case is run for 12 days at which point the waves travel across the entire sphere.

#### 5.1.6. Case 6: Cylindrical Shock Wave on a Stationary Sphere

This test case is a Riemann problem for the full nonlinear shallow water equations. A cylinder of fluid ( $h = 100\text{ m}$ ) with radius  $R = \frac{a}{3}$  is placed at  $(\lambda, \theta) = (180, 0)$ , where  $\lambda$  is longitude and  $\theta$  is latitude, with zero velocity field and no Coriolis ( $f = 0$ ). The shock wave collapses onto itself and begins to propagate through the sphere. This case is run for 5.4 days at which point the waves travel to the other side of the sphere where they collide culminating in a strong discontinuity centered at  $(\lambda, \theta) = (0, 0)$ . Slight variations of this test have been used recently for shallow water flows by Ata and Soulaïmani [1] on the plane, and Rossmanith et al. [23] on the sphere.

#### 5.1.7. Case 7: Cylindrical Shock Wave on a Rotating Sphere

This case is similar to case 6 except that we now introduce Coriolis. The rotation of the sphere vastly changes the time-evolution of the shocks. Unfortunately, this case does not have a known analytic solution.

## 5.2. Discussion of the Results

For all of the test cases we compare four versions of the high-order triangle-based DG method: the strong conservation form with  $O(2N)$  integration, the weak conservation form with  $O(2N)$  integration, the strong advection form with  $O(2N)$  integration, and the strong conservation form with  $O(2N - 1)$  integration. The difference between the  $O(2N)$  and  $O(2N - 1)$  forms is that in the former Gauss integration points are used to evaluate the flux integrals whereas in the latter Legendre-Gauss-Lobatto (LGL) integration points are used. Thus since the interpolation points of the triangle along an edge are in fact LGL points this means that the interpolation



and integration points are co-located. This allows for a very efficient evaluation of flux integrals. However, one of the questions we would like to answer is how large a loss in accuracy will be incurred by using this performance enhancing strategy. In addition, we compare the DG methods with the recently developed nodal triangle-based spectral element (SE) method with  $O(2N)$  integration given in Giraldo and Warburton [16]. We begin with three test cases with relatively simple flow.

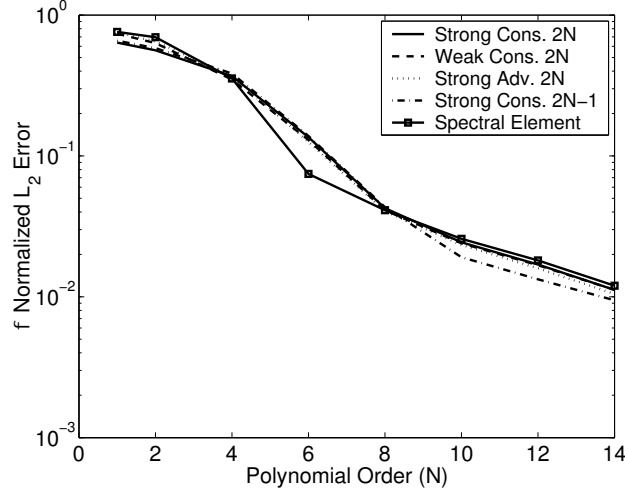


**FIG. 4.** Case 1. The normalized  $\phi$   $L_2$  error as a function of polynomial order,  $N$ , after 12 days using 80 ( $n_I = 2$ ) elements for the strong conservation form with  $O(2N)$  integration (solid line), weak conservation form with  $O(2N)$  integration (dashed line), strong advection form with  $O(2N)$  integration (dotted line), strong conservation form with  $O(2N - 1)$  integration (dashed-dotted line), and the spectral element method (solid line with square).

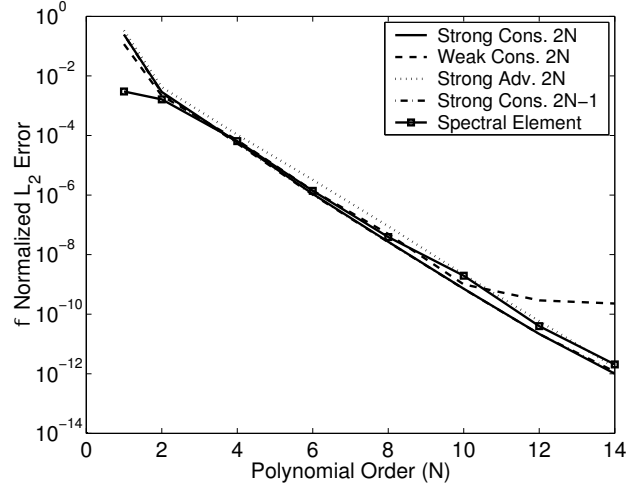
Figure 4 shows the results of case 1 as a function of polynomial order,  $N$ , for the icosahedral grid refinement level  $n_I = 2$ . The results for this test show that there is almost no difference between the four DG methods. Furthermore, the DG methods compare quite well with the SE method; the SE method gives slightly more accurate solutions near  $N = 6$  but otherwise all the methods yield similar results.

Figure 5 shows the results of case 2 as a function of polynomial order,  $N$ , for the icosahedral grid refinement level  $n_I = 2$ . For this test the strong conservation forms perform better than the weak and advection forms and the SE method. Note that the strong conservation form does quite well even when order  $O(2N - 1)$  integration is used. The weak form clearly yields the worst solution. In fact, the weak form is the only one that does not exhibit exponential convergence.

Figure 6 shows the results of case 3 as a function of polynomial order,  $N$ , for the icosahedral grid refinement level  $n_I = 2$ . For this test all the DG methods yield the same exponentially converging solution. In addition, all DG methods yield better solutions than the SE method for  $N \geq 6$ .

So far relatively insignificant differences have appeared between all four DG methods and the SE method. Cases 1, 2, and 3 are relatively smooth and thus do not pose much of a challenge for most numerical methods. The next three test cases





**FIG. 5.** Case 2. The normalized  $\phi L_2$  error as a function of polynomial order,  $N$ , after 5 days using 80 ( $n_I = 2$ ) elements for the strong conservation form with  $O(2N)$  integration (solid line), weak conservation form with  $O(2N)$  integration (dashed line), strong advection form with  $O(2N)$  integration (dotted line), strong conservation form with  $O(2N - 1)$  integration (dashed-dotted line), and the spectral element method (solid line with square).

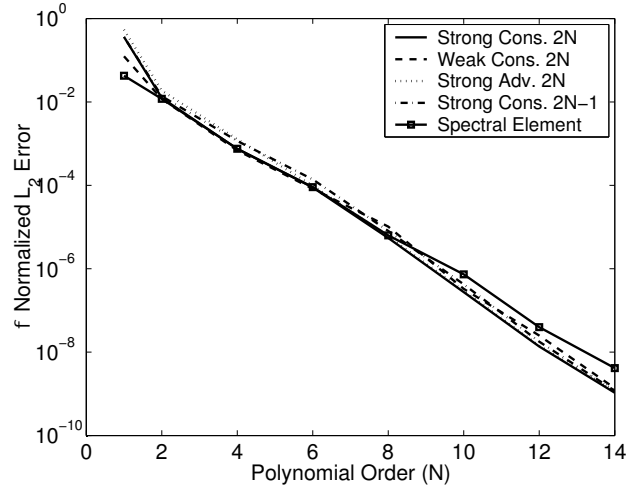
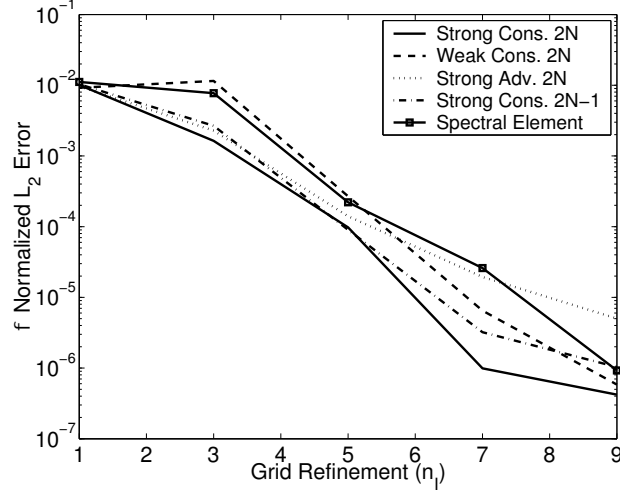


**FIG. 6.** Case 3. The normalized  $\phi L_2$  error as a function of polynomial order,  $N$ , after 5 days using 80 ( $n_I = 2$ ) elements for the strong conservation form with  $O(2N)$  integration (solid line), weak conservation form with  $O(2N)$  integration (dashed line), strong advection form with  $O(2N)$  integration (dotted line), strong conservation form with  $O(2N - 1)$  integration (dashed-dotted line), and the spectral element method (solid line with square).

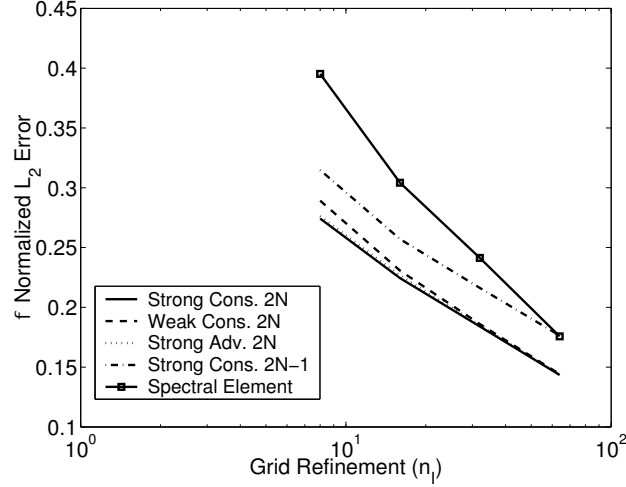
are a bit more challenging and greater differences between the four DG methods should emerge.

Figure 7 shows the results of case 4 as a function of grid refinement level,  $n_I$ , for order  $N = 8$  elements. For this test we can see that the conservation forms perform better than the weak and advection forms, and the SE method. It takes the weak form up to  $n_I = 8$  to catch up to the strong form with  $O(2N - 1)$  integration.





**FIG. 7.** Case 4. The normalized  $\phi$   $L_2$  error as a function of grid refinement,  $n_I$ , after 5 days using  $N = 8$  order elements for the strong conservation form with  $O(2N)$  integration (solid line), weak conservation form with  $O(2N)$  integration (dashed line), strong advection form with  $O(2N)$  integration (dotted line), strong conservation form with  $O(2N - 1)$  integration (dashed-dotted line), and the spectral element method (solid line with square).



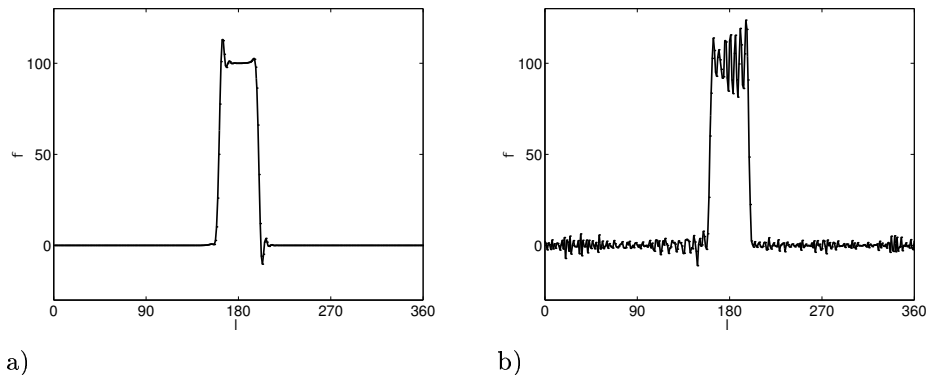
**FIG. 8.** Case 5. The normalized  $\phi$   $L_2$  error as a function of grid refinement,  $n_I$ , after 12 days using  $N = 1$  order elements for the strong conservation form with  $O(2N)$  integration (solid line), weak conservation form with  $O(2N)$  integration (dashed line), strong advection form with  $O(2N)$  integration (dotted line), strong conservation form with  $O(2N - 1)$  integration (dashed-dotted line), and the spectral element method (solid line with square).

Figure 8 shows the results of case 5 as a function of grid refinement level,  $n_I$ , for order  $N = 1$  elements. We have chosen the lowest polynomial order because since we are not using TVD schemes in the current scheme then higher order polynomials will contribute virtually nothing to the accuracy. For this test we can see that all four DG methods yield virtually similar results except for the DG with order  $O(2N - 1)$



integration. This test cases contains a scale contraction and for such problems it is very important to compute the flux integrals as accurately as possible. The similarities between the strong conservation and advection forms are not surprising because for a scalar conservation law these two forms are identical. All four DG methods perform better than the SE method; however, the SE method catches up to the DG with  $O(2N - 1)$  integration at  $n_I = 9$ .

However, showing error norms does not tell the entire story. To show the difference in the solutions between the DG and SE methods we plot the geopotential height profile along the Equator in Fig. 9 for the resolution  $n_I = 64$   $N = 1$ . The DG strong conservation form with  $O(2N)$  integration (Fig. 9a) yields a relatively smooth solution with only minimal, and more importantly, localized undershoots and overshoots; in contrast, the SE solution (Fig. 9b) experiences spurious oscillations throughout the entire domain (global influence). This difference in behavior is due to the highly localized differencing stencil of the DG method which is a direct consequence of allowing the solution across element interfaces to be discontinuous. On the other hand, the SE method requires  $C^0$  continuity across element interfaces which then allows Gibbs phenomena to pollute the entire domain during long time-integrations.



**FIG. 9.** Case 5. Profile of the geopotential height,  $\phi$ , along the Equator after 12 days for  $n_I = 64$  and  $N = 1$  for the a) DG strong conservation form with  $O(2N)$  integration and b) spectral element method.

The next few figures show results for case 6 (shock on a stationary sphere) at various times in the integration for the grid resolution  $n_I = 64$  and  $N = 1$ . This case showcases the reasons for considering DG methods over standard finite/spectral element methods. In Figs. 10, 11, and 12 we show the results as profiles of the geopotential height along the Equator as a function of longitude.

Figure 10 shows the results after a half day. The cylinder initially centered at  $\lambda = 180$  collapses onto itself forming a spike. All four DG methods yield almost identical solutions; however, there are subtle differences. The strong and weak conservation forms with  $O(2N)$  integration (Figs. 10a and 10b) yield identical results. However, the strong advection form with  $O(2N)$  integration and the strong conservation form with  $O(2N - 1)$  integration differ from the other two. The main differences are in



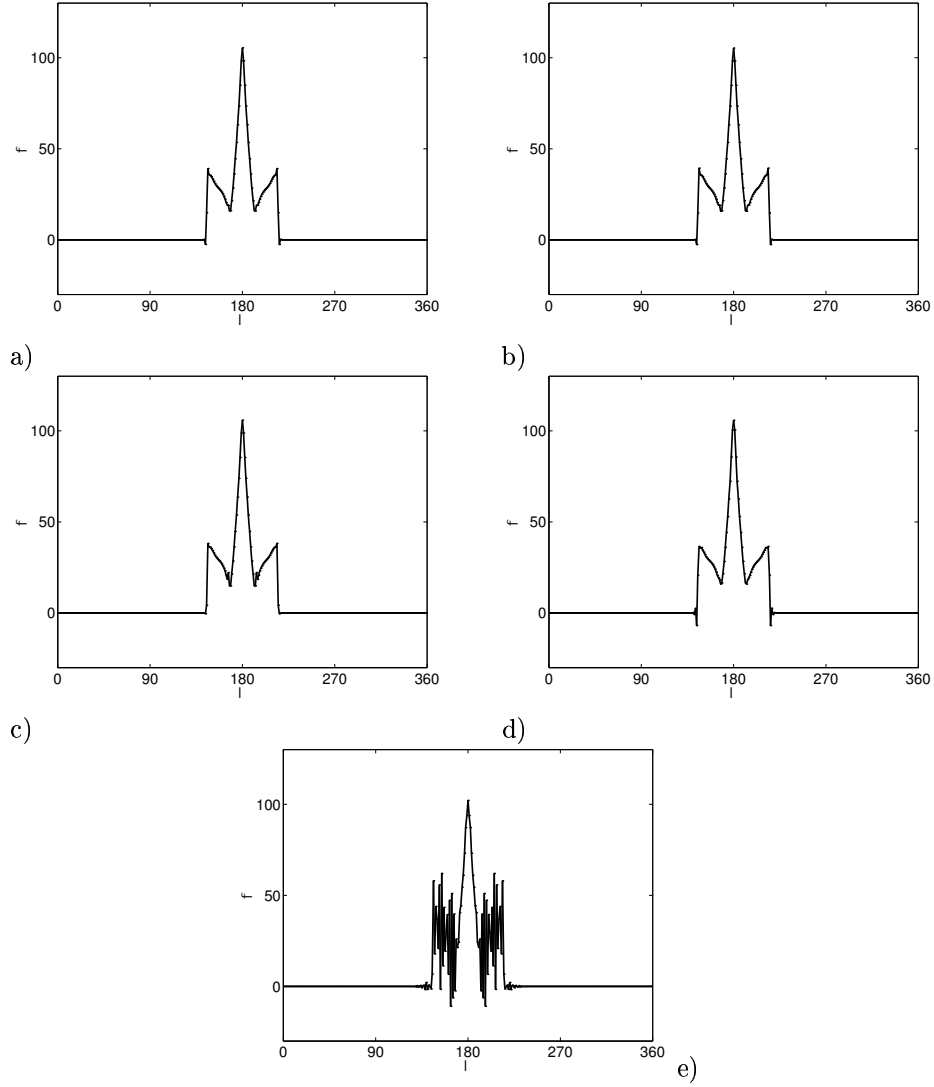


**FIG. 10.** Case 6. Profile of the geopotential height,  $\phi$ , along the Equator after 0.5 days for  $n_I = 64$  and  $N = 1$  for the a) strong conservation form with  $O(2N)$  integration, b) weak conservation form with  $O(2N)$  integration, c) strong advection form with  $O(2N)$  integration, d) strong conservation form with  $O(2N - 1)$  integration, and e) spectral element.

the slight oscillations present at the base of the spike (Fig. 10c) and at the base of the shocks (Fig. 10d). The behavior of the advection form upstream of the shocks (Fig. 10c) is very surprising. Note that there are very minimal undershoots in this region as compared to the rest of the methods. The spectral element (Fig. 10e) even with a strong filter cannot handle the shocks very well; the undershoots and overshoots severely pollute the solution. This is a good example of the spurious oscillations (Gibbs phenomena) typically exhibited by non-monotone schemes in the presence of strong discontinuities.



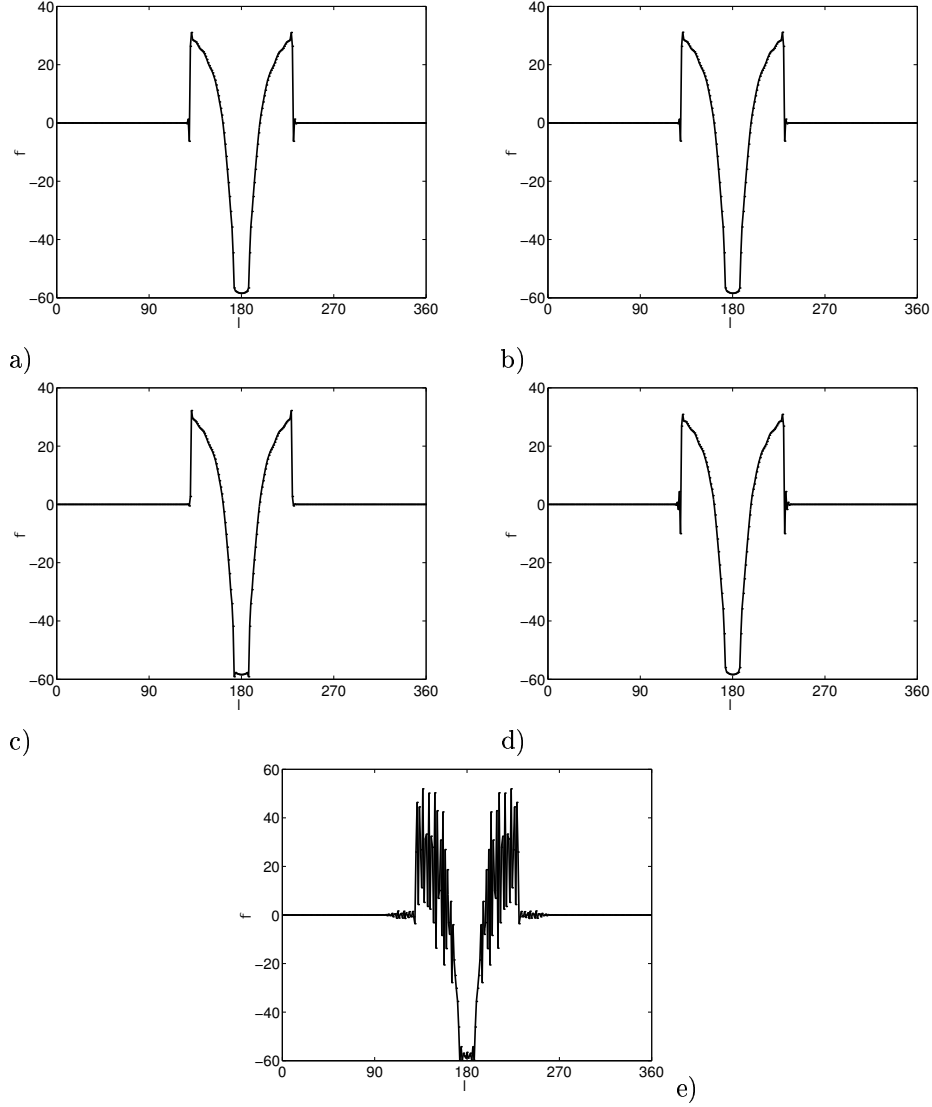
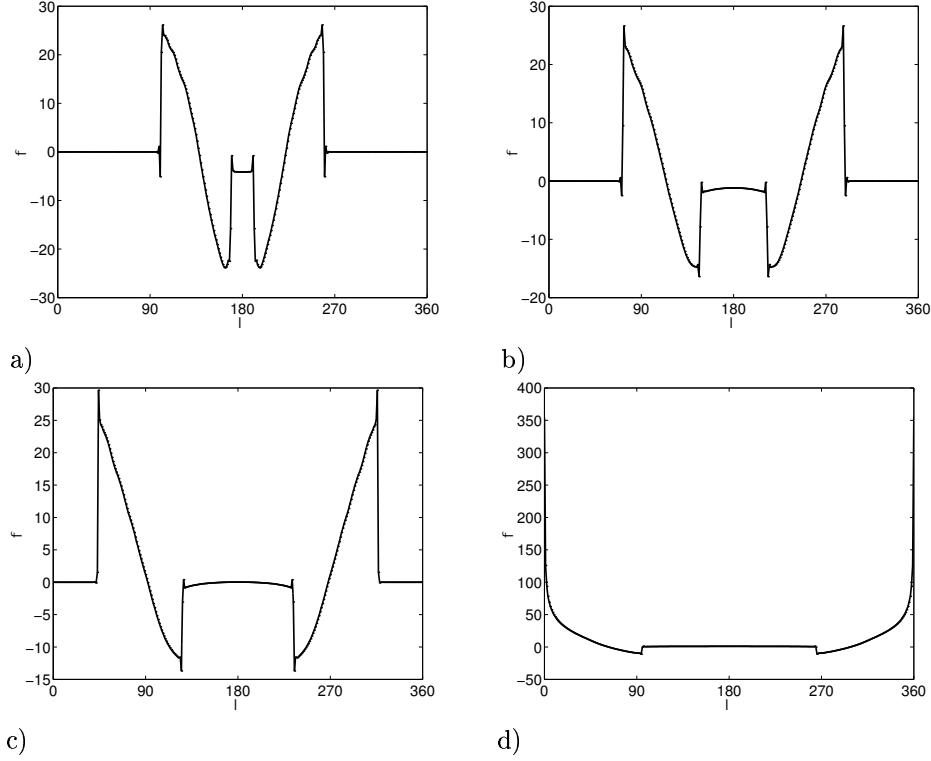


**FIG. 11.** Case 6. Profile of the geopotential height,  $\phi$ , along the Equator after 1 day for  $n_I = 64$  and  $N = 1$  for the a) strong conservation form with  $O(2N)$  integration, b) weak conservation form with  $O(2N)$  integration, c) strong advection form with  $O(2N)$  integration, d) strong conservation form with  $O(2N - 1)$  integration, and e) spectral element.

Figure 11 shows the results after 1 day. The spike formed after the first half day (Fig. 10) has now fallen below the ambient height and the two fronts of the shock race away from each other. Once again, the strong and weak conservation forms with  $O(2N)$  integration (Figs. 11a and 11b) yield identical results. The other two DG methods yield slightly different results with the strong advection form (Fig. 11c) exhibiting almost no undershoots in front of the shocks and the strong conservation form with  $O(2N - 1)$  showing larger undershoots than the other three



DG methods. The SE method once again has its solution severely polluted by the spurious oscillations in the vicinity of the shocks.



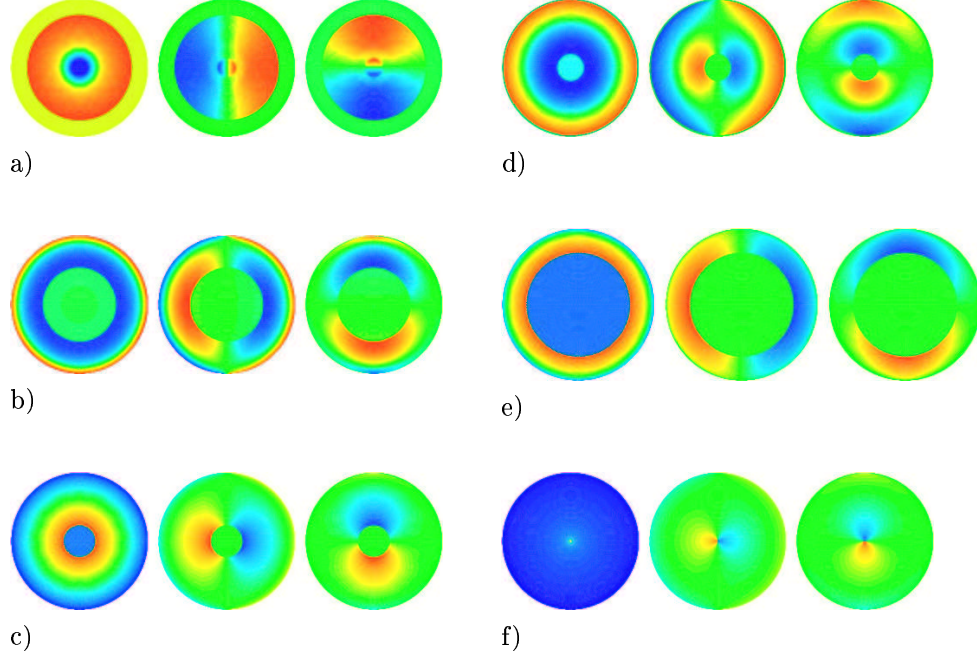
**FIG. 12.** Case 6. Profile of the geopotential height,  $\phi$ , along the Equator for the strong conservation form with  $O(2N)$  integration at times: a) 2 days, b) 3 days, c) 4 days and d) 5.4 days.

Figure 12 shows the time evolution for the strong conservation form with  $O(2N)$  integration. After 2 days (Fig. 12a) a secondary shock has formed near the initial position of the cylinder ( $\lambda = 180$ ), with the two primary shocks racing away from each other. After 3 and 4 days the primary shocks continue racing away from each other thereby widening the base of the secondary shock. Finally, after 5.4 days the primary shocks collide at  $\lambda = 0/360$  culminating in a very narrow but large spike. The jump in the secondary shock (in the range  $90 < \lambda < 270$ ) is small but clearly visible.

Snapshots of the solution contours are illustrated in Fig. 13 for various times in the integration. Figures 13a, b, and c are shown from the viewpoint  $(\lambda, \theta) = (180, 0)$  and Figs. 13d, e, and f from  $(\lambda, \theta) = (0, 0)$ . The left panel shows the geopotential height, the center panel the  $u_s$  velocity (west to east), and the right panel the  $v_s$  velocity (south to north), where the subscript  $s$  is used to remind the reader that these are the velocity components in spherical coordinates. Figure 13a shows that after 1 day the cylindrical shock wave propagates outward away from its initial position which is evident by looking at the velocity contours where



red is positive (left to right and down to up) and blue is negative. The geopotential height (left panel) shows the well that is below the ambient height (blue color); its profile can be seen more clearly in Fig. 11. Figures 13b and 13c show



**FIG. 13.** Case 6. Color contours of  $\phi$  (left),  $u_s$  (center), and  $v_s$  (right) for the DG strong conservation form with  $O(2N)$  integration for the resolution  $n_I = 64$  and  $N = 1$  at a) 1 day, b) 2 days, c) 3 days, d) 4 days, e) 5 days, and f) 5.4 days. Figures a, b, and c are viewed from  $(\lambda, \theta) = (180, 0)$  and d, e, and f from  $(\lambda, \theta) = (0, 0)$ .

the expansion of the primary shock (red) and the secondary shock (blue) after 2 and 3 days. Figures 13d and 13e show the solution after it has left this hemisphere and shows the contraction of the waves after 4 and 5 days from the view-point  $(\lambda, \theta) = (0, 0)$ . Finally, Fig. 13f shows the collision of the waves after 5.4 days which culminates in a very narrow but large spike. After 5.4 days, the large spike collapses onto itself and the shock evolution begins anew. However, beyond this point in the integration it is very difficult to discern whether the shock evolution dynamics is correct. The reason being that too many nonlinear interactions (such as colliding shocks) occur; however, the DG model has no difficulties with these dynamics and animations of 12 day integrations can be found at [www.nrlmry.navy.mil/~giraldo/projects/dg\\_tri/dg\\_tri\\_movies.html](http://www.nrlmry.navy.mil/~giraldo/projects/dg_tri/dg_tri_movies.html). It is very difficult to fully appreciate these shock dynamics without viewing the animations.

The snapshots of the solution for case 6 at various times are shown for three reasons. First, the solutions show that the grid along with the DG method retains perfect symmetry with respect to longitude and latitude throughout the integration. Second, we have tried to mimic an animation by showing the dynamics at different points in the integration. Third, these snapshots give a reference to which to



compare case 7 which is similar in every respect to this case except that the sphere rotates (Coriolis).

Snapshots of the solution contours for case 7 (shock on a rotating sphere) are illustrated in Fig. 14 for the strong conservation form with  $O(2N)$  integration. For this plot all of the views are from  $(\lambda, \theta) = (180, 0)$ , and the left panel shows the geopotential height, the center panel the  $u_s$  velocity, and the right panel the  $v_s$  velocity. Figure 14 clearly shows a different shock evolution from case 6. The addition of Coriolis vastly changes how the shock propagates. While it is very difficult to see from only viewing these snapshots, the initial cylindrical shock collapses onto itself triggering radially propagating waves which, in the absence of Coriolis would evolve as in case 6. However, the rotating sphere causes the radially outward propagating waves to fold inward which can be clearly seen in Fig. 14a. This inward folding motion causes the shock to shear into two components (Fig. 14b) which propagate in opposite directions. Note however that the eastward moving component (the right wave component on the left panel) in Fig. 14b only has a velocity component in the positive longitudinal direction (left to right) but the westward moving component is actually propagating radially. Figures 14c-f show the continued shearing of these waves which results in the long filamentations visible in Fig. 14f. It should be understood, however, that the correctness of these dynamics cannot be confirmed. We only show these results as a qualitative gage to illustrate the differences in the shock evolution when Coriolis forces are included. Animations of this test case can also be found at the previously mentioned link.

This type of simulation represents a very challenging test case for all numerical methods especially those that are being proposed for very fine-scale flows. Although the SE method we presented in [16] is exponentially convergent for smooth flows it is not so good for flows containing shocks. This is true of almost all existing methods except those that employ some form of Godunov-type method such as a Riemann solver; however, the SE method can be quite easily recast into a DG formulation such as the ones we have presented here. It should be emphasized that much better solutions (having absolutely no undershoots and overshoots) are possible with the DG method in combination with TVD flux-limiters which we reserve for future work. It is anticipated that the MUSCL-TVD methods we developed in [10, 11] for finite volume methods on unstructured triangular grids may be extended to DG formulations.

### 5.3. Computational Cost

To compare the performance of the four DG methods and the SE method we report wallclock times for case 6 for a one day integration on a Dell PC with an Intel Xeon 1.8 Gigahertz processor. Not surprisingly all of the DG methods give very similar performance with the strong conservation form with  $O(2N - 1)$  integration being the fastest. Note how much more costly is the SE method even with the aid of a state-of-the-art iterative solver (GMRES with a fast projection method, see [16]). As the grid resolution is increased this gap in performance between the SE and DG methods will continue to increase in favor of the DG methods.



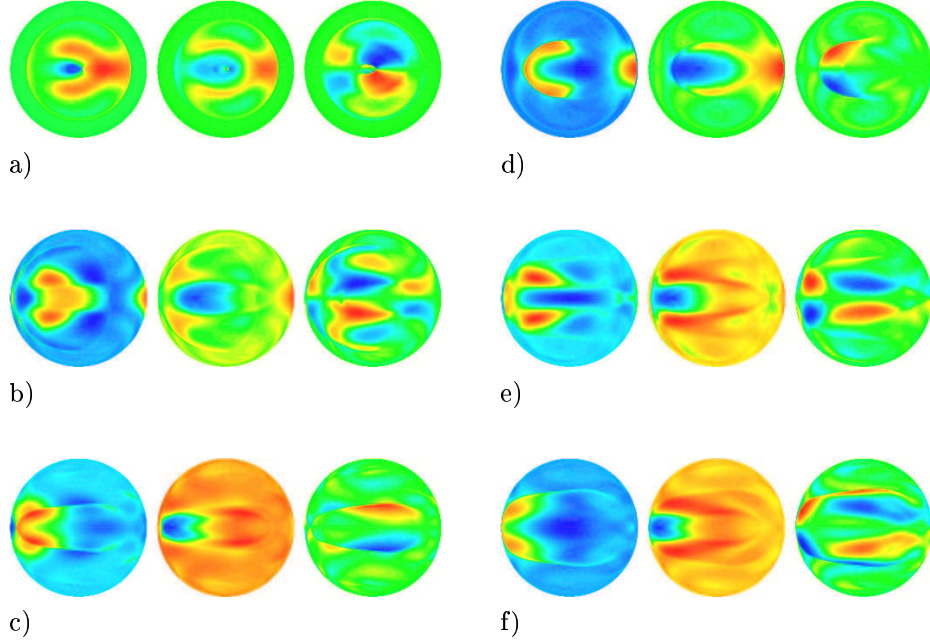


**FIG. 14.** Case 6. Color contours of  $\phi$  (left),  $u_s$  (center), and  $v_s$  (right) for the DG strong conservation form with  $O(2N)$  integration for the resolution  $n_I = 64$  and  $N = 1$  at a) 1 day, b) 2 days, c) 3 days, d) 4 days, e) 5 days, and f) 5.5 days. All the figures are viewed from  $(\lambda, \theta) = (180, 0)$ .

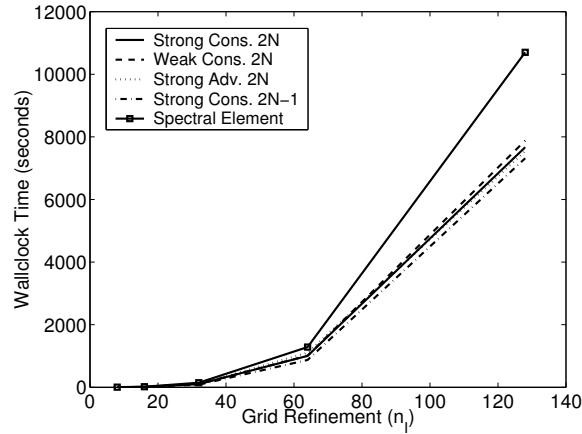


**FIG. 15.** The wallclock time required to perform a one day integration as a function of grid refinement level,  $n_I$ , using  $N = 1$  for the strong conservation form with  $O(2N)$  integration (solid line), weak conservation form with  $O(2N)$  integration (dashed line), strong advection form with  $O(2N)$  integration (dotted line), strong conservation form with  $O(2N - 1)$  integration (dashed-dotted line), and the spectral element method (solid line with square).

## 6. CONCLUSIONS

Triangle-based discontinuous Galerkin methods for flows on a rotating sphere were presented. Strong and weak conservation forms as well as the strong advec-



tion form were studied. For the test cases studied, the strong conservation form with  $O(2N)$  integration was the most robust. In general, all of the strong forms performed quite well. The weak conservation form gave similar results to the strong conservation for all cases except for one (case 2). The strong conservation form with  $O(2N - 1)$  integration performed extremely well for the cases with smooth flow (cases 1, 2, 3, and 4); however, for the case with the scale contraction (case 5) it did not do as well. Suprisingly though, for the case with the shock wave (case 6) this form performed rather well. The DG forms with  $O(2N)$  integration performed well for all the test cases.

For the test cases with smooth flow all of the DG forms gave similar or better results than the SE method with two exceptions (the weak conservation form in case 2 and the strong advection form in case 4). However, for the cases with non-smooth flows all of the DG forms gave far better results than the SE method. In addition, all of the triangle-based DG forms are more efficient than the triangle-based SE method. The reason being that for the triangle-based SE method a large global mass matrix must be inverted at every time step whereas in the DG method this mass matrix is small, local, and easy to invert.

The good results obtained with the triangle-based DG method for smooth and non-smooth flows on a rotating sphere are very exciting and in future work we plan to apply this method to other equation sets. In the current work we did not show results with adaptive grid methods but from our previous paper ([16]) it is obvious that this approach can be used immediately with the DG form. In future work, we plan to use adaptive grids in conjunction with total variation diminishing schemes for the study of shock waves on rotating spheres.

## ACKNOWLEDGMENT

FXG was supported by the Office of Naval Research through program element PE-0602435N.

## REFERENCES

1. R. Ata, and A. Soulaïmani, A stabilized SPH method for inviscid shallow water flows, *International Journal for Numerical Methods in Fluids* **47**, 139-159 (2005).
2. R. Cools, and P. Rabinowitz, Monomial cubature rules since Stroud: A compilation, *Journal of Computational and Applied Math*, **48**, 309-326, (1993).
3. R. Cools, Monomial cubature rules since Stroud: A compilation - Part 2, *Journal of Computational and Applied Math*, **112**, 21-27, (1999).
4. P.J. Diamessis, J.A. Domaradzki, and J.S. Hesthaven, A spectral multidomain penalty method model for the simulation of high Reynolds number localized incompressible stratified turbulence, *Journal of Computational Physics* **202**, 298-322 (2005).
5. M. Dubiner, Spectral methods on triangles and other domains, *Journal of Scientific Computing* **6**, 345-390 (1991).
6. F. Dupont and C.A. Lin, The adaptive spectral element method and comparisons with more traditional formulations for ocean modeling, *Journal of Atmospheric and Oceanic Technology* **21**, 135-147 (2004).
7. C. Eskilsson, and S.J. Sherwin, A triangular spectral/hp discontinuous Galerkin method for modelling 2D shallow water equations, *International Journal for Numerical Methods in Fluids* **45**, 605-623 (2004).
8. O. Friedrich, Weighted essentially non-oscillatory schemes for the interpolation of mean values on unstructured grids, *Journal of Computational Physics* **144**, 194-212 (1998).
9. J. Galewsky, R.K. Scott, and L.M. Polvani, An initial-value problem for testing numerical models of the global shallow water equations, *Tellus* **56**, 429-440 (2004).



10. F.X. Giraldo, *A space marching adaptive remeshing technique applied to the 3D Euler equations for supersonic flow*, PhD thesis, University of Virginia (1995).
11. F.X. Giraldo, A finite volume high resolution 2D Euler solver with adaptive grid generation on high performance computers, *Proceedings of the 9th International Conference on Finite Element in Fluids*, M. Morandi-Cecchi, K. Morgan, J. Periaux, B.A. Schrefler, and O.C. Zienkiewicz (eds.), Venice Italy (1995).
12. F.X. Giraldo, A spectral element shallow water model on spherical geodesic grids, *International Journal for Numerical Methods in Fluids* **35**, 869-901 (2001).
13. F.X. Giraldo, J.S. Hesthaven, and T. Warburton, Nodal high-order discontinuous Galerkin methods for the spherical shallow water equations, *Journal of Computational Physics* **181**, 499-525 (2002).
14. F.X. Giraldo, J.B. Perot, and P.F. Fischer, A spectral element semi-Lagrangian (SESL) method for the spherical shallow water equations, *Journal of Computational Physics* **190**, 623-650 (2003).
15. F.X. Giraldo, Semi-implicit time-integrators for a scalable spectral element atmospheric model *Quarterly Journal of the Royal Meteorological Society* in press (2005).
16. F.X. Giraldo, and T. Warburton, A nodal triangle-based spectral element method for the shallow water equations on the sphere, *Journal of Computational Physics* in press (2005).
17. J.S. Hesthaven, From electrostatics to almost optimal nodal sets for polynomial interpolation in a simplex, *SIAM Journal on Numerical Analysis* **35**, 655-676 (1998).
18. C.Q. Hu and C.W. Shu, Weighted essentially non-oscillatory schemes on triangular meshes *Journal of Computational Physics* **150**, 97-127 (1999).
19. G.E. Karniadakis, M. Israeli, and S.A. Orszag, High-order splitting methods for the incompressible Navier-Stokes equations, *Journal of Computational Physics* **97**, 414-443 (1991).
20. T. Koornwinder, Two-variable analogues of the classical orthogonal polynomials, in *Theory and Applications of Special Functions*, edited by A.R.A. (Academic Press, San Diego, 1975).
21. J. Lyness and R. Cools, A survey of numerical cubature over triangles, *Applied Mathematics* **48**, 127-150 (1994).
22. J. Proriot, Sur une famille de polynomes á deux variables orthogonaux dans un triangle, *C.R. Acad. Sci Paris* **257** 2459 (1957).
23. J.A. Rossmanith, D.S. Bale, and R.J. LeVeque, A wave propagation algorithm for hyperbolic systems on curved manifolds, *Journal of Computational Physics* **199**, 631-662 (2004).
24. C.W. Shu, High-order finite difference and finite volume WENO schemes and discontinuous Galerkin methods for CFD, *International Journal of Computational Fluid Dynamics* **17**, 107-118 (2003).
25. A.H. Stroud, *Approximate Calculation of Multiple Integrals*, Prentice-Hall Publishing, New Jersey, (1971).
26. M.A. Taylor, B.A. Wingate, and R.E. Vincent, An algorithm for computing Fekete points in the triangle, *SIAM Journal on Numerical Analysis* **38**, 1707-1720 (2000).
27. E.F. Toro, *Riemann Solvers and Numerical Methods for Fluid Dynamics, A Practical Introduction*, Springer (New York, 1999).
28. D.L. Williamson, J.B. Drake, J.J. Hack, R. Jakob, and P.N. Swarztrauber, A standard test set for numerical approximations to the shallow water equations in spherical geometry, *Journal of Computational Physics* **102**, 211-224 (1992).